Nano Res (2009) 2: 151–160
DOI 10.1007/s12274-009-9014-y
Research Article

Synthesis and Purple-Blue Emission of Antimony Trioxide Single-Crystalline Nanobelts with Elliptical Cross Section

Zhengtao Deng[1,2,3], Dong Chen[1], Fangqiong Tang[1] (✉), Jun Ren[1], and Anthony J. Muscat[2]

[1] Laboratory of Controllable Preparation and Application of Nanomaterials, Technical Institute of Physics and Chemistry, Chinese Academy of Sciences, Beijing 100080, China
[2] Department of Chemical and Environmental Engineering, The University of Arizona, Tucson, Arizona 85721, USA
[3] College of Optical Science, The University of Arizona, Tucson, Arizona 85721, USA

Received: 13 October 2008 / Revised: 15 December 2008 / Accepted: 15 December 2008
©Tsinghua University Press and Springer-Verlag 2009. This article is published with open access at Springerlink.com

ABSTRACT

Single-crystalline orthorhombic antimony trioxide (Sb_2O_3) nanobelts with unique elliptical cross sections and purple-blue photoluminescence have been synthesized. The uniform Sb_2O_3 nanobelts are 400–600 nm in width, 20–40 nm in thickness at the center and gradually become thinner to form sharp edges sub-5 nm in size, tens of micrometers in length, and with [001] as the preferential growth direction. Self-assembly of tens of nanobelts into three-dimensional (3-D) flower-like nanostructures has been observed. Analysis was performed by X-ray diffraction, energy-dispersive X-ray spectroscopy, X-ray photoelectron spectroscopy, scanning electron microscopy, high-resolution transmission electron microscopy, selected area electron diffraction, Raman spectroscopy, Fourier transform infrared spectroscopy, and photoluminescence spectroscopy. The Sb_2O_3 nanobelts display intense purple-blue photoluminescence centred at 425 nm (~2.92 eV). The successful synthesis of nanobelts with elliptical cross sections may cast new light on the investigation of the property differences between nanobelts with rectangular cross sections and those with other cross section geometries. The Sb_2O_3 nanobelts can be used as effective purple-blue light emitters and may also be valuable for future nanodevice design.

KEYWORDS

Antimony trioxide, nanobelts, elliptical cross section, purple-blue, photoluminescence

Introduction

Since the discovery of nanobelts of semiconducting oxides in 2001 [1], nanobelts have attracted considerable attention due to their dimensionally confined and structurally well-defined physical and chemical properties, and their potential applications in nanodevices such as field effect transistors, ultrasensitive gas sensors, resonators, and cantilevers [2–8]. Generally, nanobelts have a rectangular cross section and well-defined faceted surfaces [4]. ZnO nanobelts with rectangular cross sections have been used as effective Fabry–Perot microcavities for lasing [9]. Recent research suggests that, in addition to size and dimension, the cross section also has a shape effect on the properties of nanomaterials [10].

Address correspondence to: tangfq@mail.ipc.ac.cn

According to classical waveguide theory, waveguides with different cross sections will exhibit different transverse optical modes [4]. Therefore, the synthesis of metal oxide semiconductor nanobelts with cross sections other than rectangular is an urgent requirement for both fundamental research and technological application.

Recently, integration of one-dimensional (1-D) nanostructures—such as nanowires and nanobelts —into two- and three-dimensional (2-D and 3-D) hierarchical nanostructures or complex functional architectures, which are essential for the success of bottom-up approaches toward advanced materials and devices, has been one of the challenging issues faced by chemists [11–16]. To date, simple 1-D Sb_2O_3 nanostructures such as nanorods, nanowires, nanotubes, and nanoribbons have been synthesized via a variety of processes [17–24]. For example, O'Brien et al. [22] reported that refluxing antimony acetate with octylamine afforded Sb_2O_3 nanostructures. More recently, Sendor et al. [23] synthesized Sb_2O_3 nanoribbons with lengths up to 15 μm and diameters ranging between 8 and 50 nm by a solid-to-nanostructure transformation route. However, Sb_2O_3 3-D nanostructures built up from simple 1-D nanowires or nanobelts have not been obtained so far.

An important member of the class of functional metal oxides, Sb_2O_3 has been widely used as a fire retardant, a filler, a catalyst, and in pH electrodes [25–28]. Similar to other well-studied functional metal oxides, Sb_2O_3 is also expected to be an interesting semiconducting material exhibiting unique optical, electronic, and optoelectronic properties. Recently, our group has reported the room temperature ultraviolet band-edge photoluminescence centered at 374 nm for Sb_2O_3 single crystalline nanowires [24]. More studies are still needed to explore the optical and electronic properties of various Sb_2O_3 nanostructures in order to fully understand the nature of Sb_2O_3.

Herein, the synthesis of single-crystalline Sb_2O_3 nanobelts with unique elliptical cross sections and their self-assembly into 3-D flower-like nanostructures is described. The advantages of the present work are the following: (1) Uniform well-crystallized single-crystalline Sb_2O_3 nanobelts with unique elliptical cross sections have been synthesized; to our knowledge, nanobelts with elliptical cross sections have not been reported previously. (2) Sb_2O_3 3-D nanostructures built up from simple 1-D nanobelts were achieved; this is the first synthesis of 3-D nanostructures of Sb_2O_3. (3) The new Sb_2O_3 nanobelts exhibited intense purple-blue photoluminescence centered at 425 nm.

1. Experimental

Our group has developed a strategy for the synthesis of various oxide and oxyhalide nanostructures such as Sb_2O_3, SnO_2, BiOCl, and BiOBr, by a facile route involving direct air oxidation of bulk metal particles in a mixed solution of ethylenediamine (EA) and deionized water (DIW) [29–32]. The synthesis processes for Sb_2O_3 nanobelts with elliptical cross sections and their flower-like nanostructures followed this strategy but with alteration of the experimental parameters. In a typical experiment, 120 mg Sb powder (<200 mesh, 99.5%), 400 mg polyvinylpyrrolidone (PVP, MW 30000) and 15 mmol EA, were added to 74 mL DIW. The mixed solution was first stirred at 60 °C for 1 h and then kept at room temperature without disturbance for about 72 h. After the reaction, the resulting white solid product was filtered and washed with DIW and ethanol to remove residual ions in the product. The final product was then dried in air at 60 °C for 4 h before characterization.

X-ray powder diffraction (XRD) measurements employed a Rigaku D/max γA X-ray diffractometer equipped with graphite monochromatized Cu Kα radiation (λ =1.5418 Å) with a scanning rate of 0.02 (°)/s. Scanning electron microscopy (SEM) and energy-dispersive X-ray spectroscopic (EDS) measurement were performed using a Hitachi S-4300 scanning electron field emission microscope operating at 15 kV. X-ray photoelectron spectroscopy (XPS) was performed using an achromatic Al Kα source (1486.6 eV) and a double pass cylindrical mirror analyzer (Physical Electronics 549). Survey and high-resolution spectra were recorded at pass energies of 200 and 50 eV, respectively. Peak fitting was performed using multi-peak fitting packages

included with Igor Pro (WaveMetrics, Inc., v.6). The atomic ratios were obtained from ratios of XPS peak areas in the high-resolution spectra corrected by sensitivity factors from the Ref. [33]. Transmission electron microscopy (TEM), high-resolution TEM (HRTEM), and selected area electron diffraction (SAED) patterns were performed on a JEOL JEM-2010 electron microscope operating at 200 kV. Micro-Raman experiments were conducted in a Raman scattering spectrometer (LabRAM HR, HORIBA Jovin Yvon), with the 514.5 nm line of an Ar^+ laser as the excitation source. Fourier transform infrared (FT-IR) spectra were recorded with a Varian 3100 FT-IR spectrometer at room temperature. Photoluminescence (PL) spectra were measured with a Hitachi F4500 fluorescence spectrophotometer at room temperature.

2. Results and discussion

Figure 1(a) shows a typical XRD pattern of the as-synthesized product. All the diffraction peaks of the sample can be readily indexed as the orthorhombic phase of Sb_2O_3 (cell constants a=4.911 Å, b=12.464 Å, c= 5.412 Å; JCPDS Card No. 11-0689). No peaks from metallic Sb or any other phases are detected. In addition, the intense and sharp diffraction peaks suggest the as-synthesized product is well crystallized. Furthermore, the (110) and the (200) peak intensities are significantly enhanced, and the (121) and the (131) peak intensities are considerably decreased relative to bulk orthorhombic phase valentinite, indicating the preferred crystallographic orientation of the product. To determine the composition of the product, EDS was performed on an individual nanobelt, as shown in Fig. 1(b). Only Sb and O peaks are observed in the spectrum (the Si signal arises from the silicon substrate), suggesting that the product is composed of Sb and O. Quantitative EDS analysis shows that the atom ratio Sb : O is 39 : 61, close to 2 : 3, indicating the composition of the as-synthesized product is Sb_2O_3.

The survey XPS spectrum shown in Fig. 2(a) indicates that the nanobelts contain Sb, O, and C. Surface charging was corrected by referencing the spectra to the C–C state of the C 1s peak at a binding

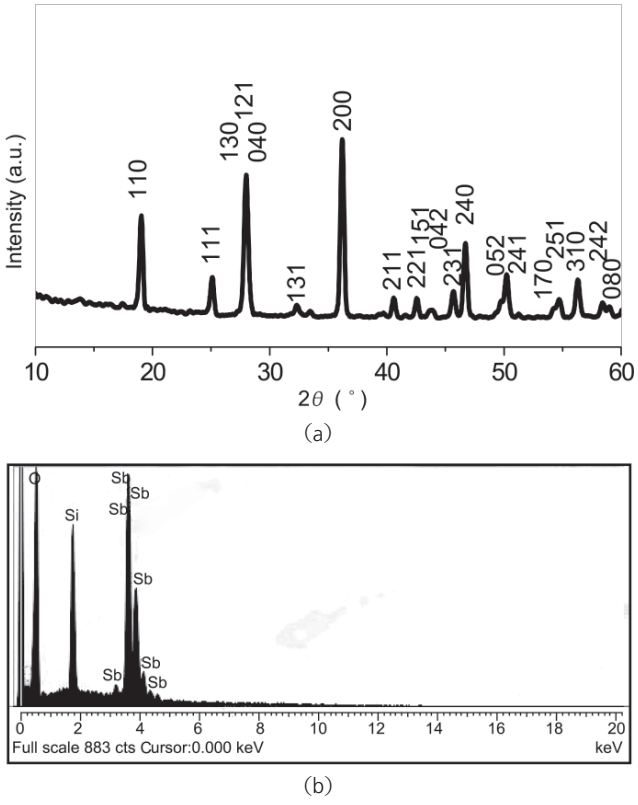

Figure 1 (a) XRD and (b) EDS patterns of Sb_2O_3 nanbelts

energy of 284.5 eV. Since the Sb $3d_{5/2}$ region overlaps with the O 1s region, peak fitting was performed for the high-resolution XPS spectra as shown in Fig. 2(b). The Sb 3d spectrum exhibited two peaks: One at 539.2 eV, which was assigned to Sb $3d_{3/2}$, and one at 529.9 eV, which was assigned to Sb $3d_{5/2}$. The two peaks are due to spin–orbit coupling of the 3d state with a spin–orbit separation of 9.3 eV and a spin–orbit branching ratio of 1.67, which agrees well with that reported previously for Sb_2O_3 [34, 35]. The Sb $3d_{3/2}$ region showed a single peak at a binding energy of 539.2 eV, indicating that the sample was composed of only the Sb(III) state, with no significant amounts of Sb(0), which is expected at 537.6 eV, nor Sb(V), which occurs at 540.3 eV. The O 1s region shown in Fig. 2(b) contained a single symmetric peak at 528.5 eV assigned to O in Sb_2O_3. The shift to lower binding energy compared to other oxide species shows that the Sb–O bond is primarily ionic. The total Sb : O ratio computed on the basis of peak areas and sensitivity factors is about 0.63; this value is also consistent with the composition Sb_2O_3.

SEM images shown in Figs. 3(a)–3(d) and the

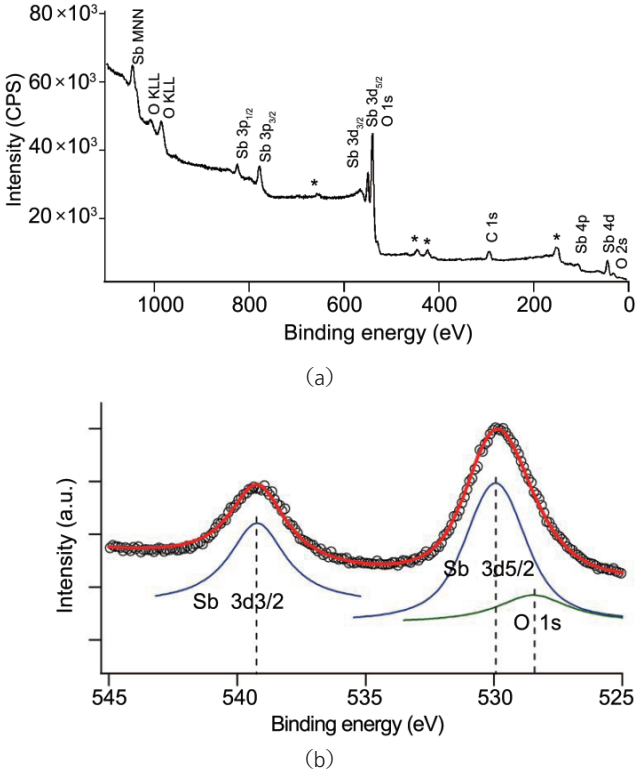

Figure 2 (a) Survey X-ray photoelectron spectrum of Sb_2O_3 nanobelts; (b) high-resolution X-ray photoelectron spectra of Sb_2O_3 nanobelts in the Sb and O regions. Note the small peaks marked by * come from the lead from the substrate

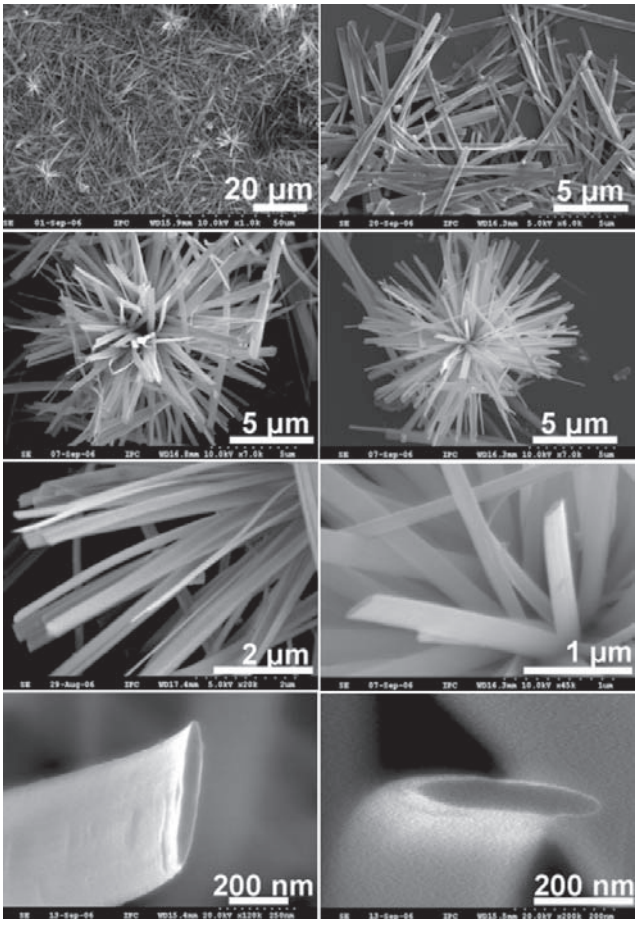

Figure 3 (a) Low-magnification SEM image of the Sb_2O_3 product; (b) SEM image of the individual nanobelts; (c), (d) SEM images of Sb_2O_3 nanobelts self-assembled into 3-D flower-like nanostructures; (e), (f) high-magnification SEM images of the nanobelts incorporated in the 3-D nanostructures; (g), (h) high-magnification SEM images of the tips of the cross-sections of the nanobelts

Electronic Supplementary Material (ESM) reveal that the as-synthesized product is composed of a large quantity of individual nanobelts together with 3-D flower-like nanostructures made up of dense assemblies of numerous individual nanobelts. High-magnification SEM images (see Figs. 3(e), 3(f), and the ESM) show that the Sb_2O_3 nanobelts are very highly uniform. Most of the individual nanobelts were 400–600 nm in width and tens of micrometers in length. Closer inspection revealed that the 1-D nanobelts appeared to have an ideal belt-like morphology with elliptical cross sections, i.e., 20–40 nm in thickness at the center and gradually becoming thinner to form sharp edges sub-5 nm in size (see Figs. 3(g), 3(h), and the ESM). Eklund et al. [10] pointed out that the cross section also has a shape effect on the properties of nanomaterials in addition to their size and dimensions. In addition, waveguides of different cross sections will exhibit different transverse optical modes [4]. Therefore, the unique structure of the nanobelts with elliptical cross sections is likely to give an ideal materials family for a systematic experimental and theoretical study of the fundamental electrical, optical, and thermal transport processes in 1-D nanostructures. It should be pointed out that most previously reported nanobelts have rectangular cross sections [1–4], and our report is the first demonstration that nanobelts can have elliptical cross sections. Thus, our results may cast new light on the investigation of property differences between nanobelts with rectangular cross sections and those with cross sections of other geometries.

The morphologies of the as-synthesized product were further investigated by TEM as shown in Figs. 4(a)–4(d) , which also show that individual nanobelts and the 3-D flower-like nanostructures are built up of numerous individual Sb_2O_3 nanobelts, consistent

with the SEM observations. The microstructure of an individual Sb_2O_3 nanobelt (see Fig. 4(e)) was further investigated in detail by HRTRM and SAED. A typical HRTEM image of a single Sb_2O_3 nanobelt is shown in Fig. 4(f). The central part of the nanobelt, shown in Fig. 4(i), gives lattice spacings of about 1.246 and 0.271 nm, corresponding to the (010) and (002) planes of orthorhombic phase Sb_2O_3 (JCPDS Card No. 11-0689), respectively. In contrast, the edge part of the nanobelt (Fig. 4(j)) gives lattice spacings of about 0.312 and 0.271 nm, corresponding to the (040) and (002) planes of orthorhombic phase (JCPDS Card No. 11-0689), respectively. The differences between the HRTEM images might be attributable to the surface of the single nanobelt not being flat, i.e., having a curve or arch-like morphology. The SAED pattern shown in the inset to Fig. 4(f) is a spot pattern, which reveals that the nanobelt is single crystalline in nature. The corresponding indexed fast Fourier transforms (FFTs) of the same areas show similar patterns to the SAED, indicating the formation of high quality single-crystal orthorhombic Sb_2O_3 nanobelts. Both the HRTEM image and SAED pattern demonstrate that the nanobelts grow along the [001] direction (indicated with an arrow in Fig. 4(e)).

As shown in Fig. 5, the product shows peaks in the room temperature Raman spectrum at 142, 190, 219, 290, 439, 499, 595, and 679 cm^{-1}, which fit well with those reported by Cody et al. [36] (141, 189, 219, 295, 500, 596, and 690 cm^{-1}) for the orthorhombic Sb_2O_3 phase. Orthorhombic Sb_2O_3 crystallizes in the space group Pccn (D_{2h}^{10}) and is built up of infinite polymeric Sb–O–Sb chains running along the *c* axis with Sb–O distances of 0.200 nm. The Raman spectrum in the internal mode region (400–800 cm^{-1}) of orthorhombic Sb_2O_3 is mainly dependent on the spectral features of the polymeric Sb–O chains. The lattice mode region (below 400 cm^{-1}), however, is controlled by the crystal space group and unit cell coupling [24, 37]. Thus, all signals below 400 cm^{-1} belong to the external lattice mode regime, while those above 400 cm^{-1} belong to the internal vibrations. In addition, we found that the Raman spectrum of the product calcined at 400°C for 3 h in air was almost identical to the uncalcined product, suggesting that the Sb_2O_3 nanobelts obtained from the solution at low temperature are well-crystallized.

As shown in Fig. 6, the FT-IR spectra indicate

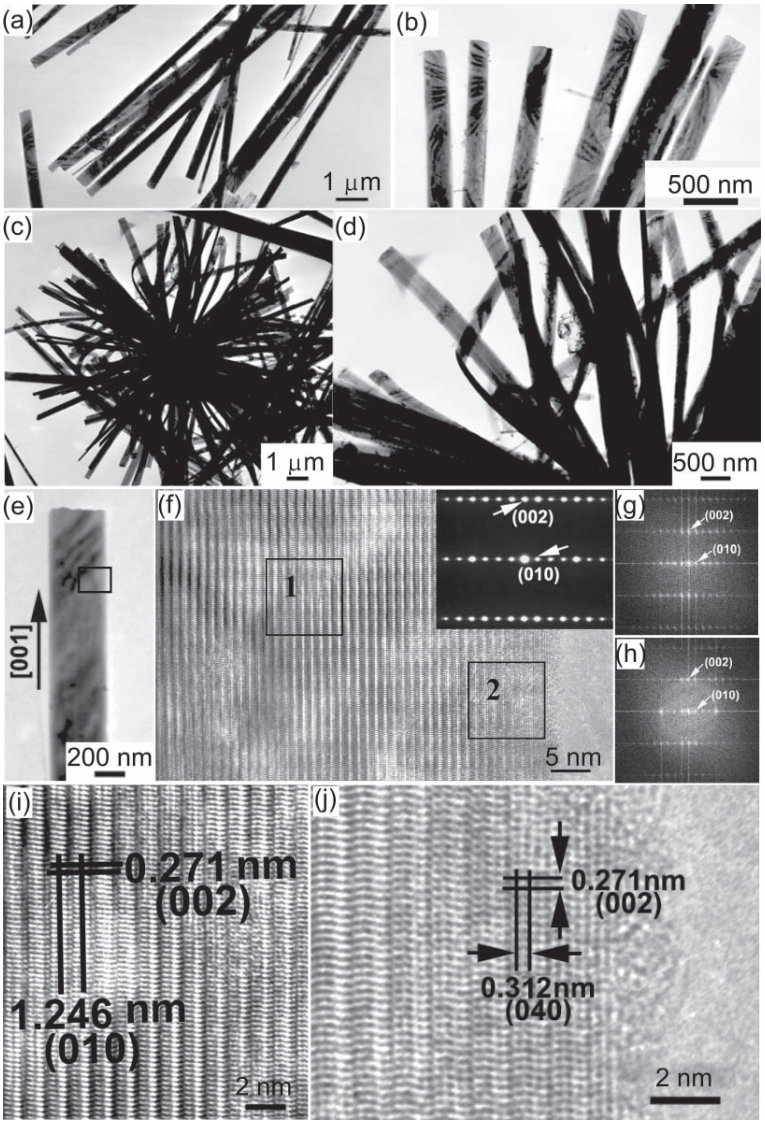

Figure 4 (a), (b) TEM images of Sb_2O_3 nanobelts; (c), (d) TEM images of the nanobelts self-assembled into 3-D flower-like nanostructures; (e) TEM image of an individual Sb_2O_3 nanobelt incorporated in the 3-D flower-like nanostructure; (f) HRTEM image of the part of the Sb_2O_3 nanobelt marked by a rectangle in (c) and (inset) the corresponding SAED pattern; (g), (i) indexed fast Fourier transforms (FFTs) and enlarged HRTEM image of the square area marked "1" in (f); (h), (j) indexed FFTs and enlarged HRTEM image of the square area marked "2" in (f)

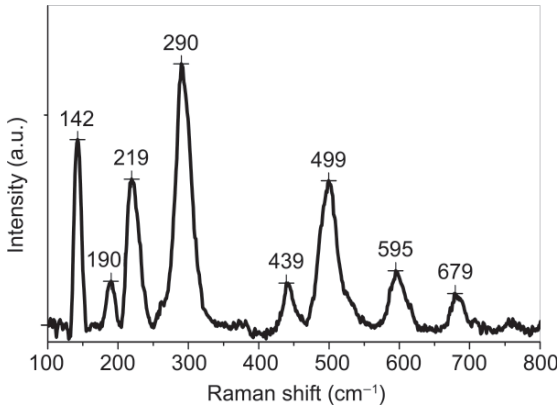

Figure 5 Room temperature Raman spectrum of the Sb_2O_3 nanobelts

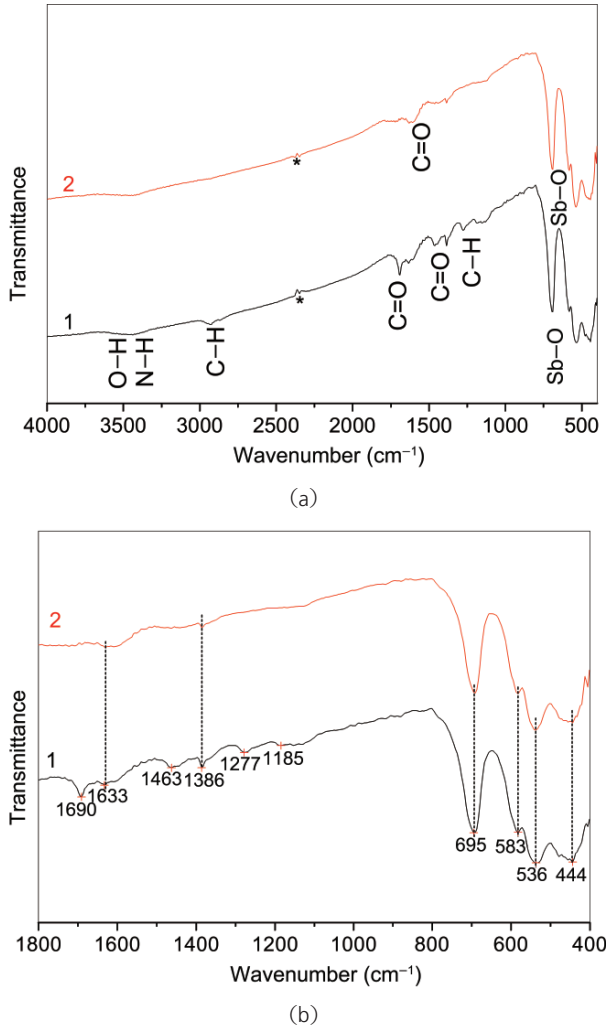

Figure 6 Room temperature FT-IR spectra of the Sb_2O_3 nanobelts (1) before and (2) after calcination: (a) in the range 4000–400 cm^{-1} and (b) in the range 1800–400 cm^{-1}. Note the peaks marked by * come from CO_2 in the environment

that as-synthesized Sb_2O_3 nanobelt samples display very weak absorption peaks at 1185, 1277, 1463, and 2929 cm^{-1} which are associated with the characteristic C–H vibrations coming from traces of ethylenediamine and polyvinylpyrrolidone in the product. The peaks at 1386, 1633, and 1690 cm^{-1} are characteristic of C=O stretching, and may arise from traces of polyvinylpyrrolidone. The peak at 3470 cm^{-1} is characteristic of N–H and O–H stretching, consistent with traces of ethylenediamine or water being present. The low wavenumber region 400–800 cm^{-1} depicts the lattice vibrations of Sb_2O_3; peaks were observed at 444, 536, 583, and 695 cm^{-1} corresponding to symmetric and antisymmetric Sb–O–Sb vibrations [24, 36]. The as-synthesized nanobelts could be further purified by calcination. After being calcined at 400 °C for 3 h in the air, most of the peaks attributed to traces of ethylenediamine, polyvinylpyrrolidone, and water were eliminated; however, the intensity of the Sb–O–Sb vibration peaks remained unchanged.

The growth mechanism of nanobelts with rectangular cross sections can be explained by the different growth rates of various crystal facets [1–4, 24], but the growth mechanism of the nanobelts with elliptical cross sections is harder to understand. As the synthesis takes place in aqueous solution, the growth of Sb_2O_3 nanobelts with elliptical cross sections may be analyzed in terms of local thermodynamic equilibrium theory and concluded to be the result of the co-effects of the energy of surface tension and the energy of the crystal facets. Generally, the former tends to make the surface of the crystals round due to the associated reduction in surface area, while the latter tends to make it faceted due to the orthorhombic structure of Sb_2O_3. In addition, an "Ostwald ripening" effect may transform initially formed nanobelts with rectangular cross section into the final nanobelts with elliptical cross sections as the product was kept without disturbance for a period as long as 72 h. The exact growth mechanism of the nanobelts with elliptical cross section is currently under investigation in our laboratory. The formation process of the 3-D flower-like nanostructures can be explained in terms of an organizing principle with an oriented attachment mechanism in which

complex architectures can be built by the assembly route: 0-D → 1-D → 3-D [14–16]. Since metallic Sb particles are employed as the source, we assume that the preformed Sb_2O_3 oxide layer on the pristine Sb particles is crucial to the success of initial nucleation and the subsequent growth of 1-D nanostructures on the surface of the Sb particles. The experimental parameters such as temperature and amount of EA play an important role in the formation of Sb_2O_3 nanobelts with elliptical cross sections. Our previous study [24] showed that uniform, single-crystalline, well-faceted Sb_2O_3 nanowires with rectangular cross sections with lengths of hundreds of micrometers , typically 80–100 nm in width and 60–80 nm in thickness could be synthesized in a much shorter time of 5 h at room temperature. As shown in Fig. 7, the SEM images indicated that if the temperature was increased to 100 °C, while keeping the other experimental parameters the same as for the synthesis of the Sb_2O_3 nanobelts, the resulting product is composed of micrometer-scale wires with rectangular cross-sections with lengths up to 50 μm and average thickness around 2 μm. This growth process of Sb_2O_3 3-D flower-like nanostructures is similar to the formation of ZnO nanoflowers from metallic Zn particles [38], which involves a surfactant-assisted solid-solution-solid mechanism [39, 40]. In addition, similar nanobelts involving self-assembled nanostructures of cobalt phosphate have been synthesized by a hydrothermal reaction [41].

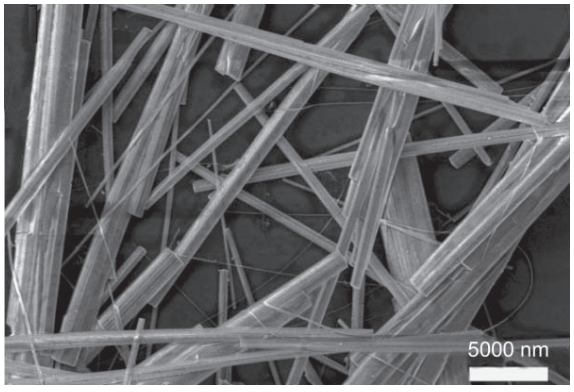

(a)

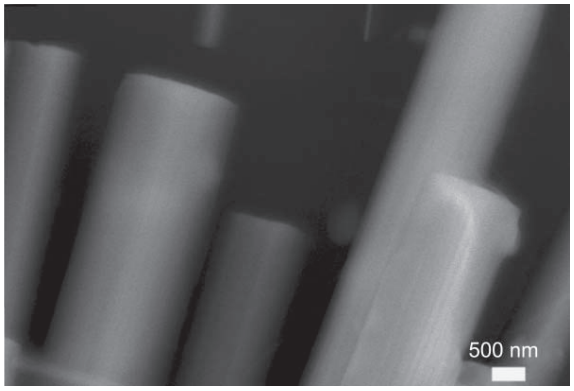

(b)

Figure 7 SEM images of Sb_2O_3 micrometer-scale wires with rectangular cross section synthesized at 100 °C

Figure 8(a) shows the excitation spectrum of Sb_2O_3 nanobelts with the emission monitored at 425 nm. Three excitation peaks at 365 nm (strong peak), 348 nm (weak shoulder peak), and 380 nm (weak shoulder peak) can be observed in the excitation spectrum. As shown in Fig. 8(b), the photoluminescence spectrum of Sb_2O_3 nanobelts using an excitation wavelength of 365 nm shows an intense purple-blue emission at 425 nm (~2.92 eV) with a full width at half maximum (FWHM) of 75 nm (0.47 eV). We have also examined the emission spectra of the nanostructures excited under different wavelengths—325 nm, 348 nm, 375 nm, 390 nm, and 395 nm. It can be seen that the emission peak positions of the product remain almost unchanged under different excitation wavelengths, showing is an intrinsic property of the Sb_2O_3 nanobelts themselves. The photoluminescence spectra of the calcined Sb_2O_3 nanobelts samples were identical to those of the uncalcined samples as shown in Fig. 8(a). It is worth noting that room temperature ultraviolet (UV) band-edge photoluminescence with a peak at 374 nm has previously been observed for Sb_2O_3 nanowires [24]. The purple-blue photoluminescence at 425 nm (~2.92 eV) is probably due to a triplet to ground transition of a neutral oxygen vacancy defect, as suggested by *ab initio* molecular orbital calculations for many other well-studied metal oxides such as ZnO and SnO_2 [42, 43]. Considering that the energy gap of bulk Sb_2O_3 is 3.3 eV, the purple-blue luminescence from Sb_2O_3 nanobelts can be attributed to oxygen-related defects that have been introduced during growth. The interactions between oxygen vacancies and interfacial antimony vacancies would lead to the formation of a significant number of trapped states, which form a series of metastable energy levels within the band

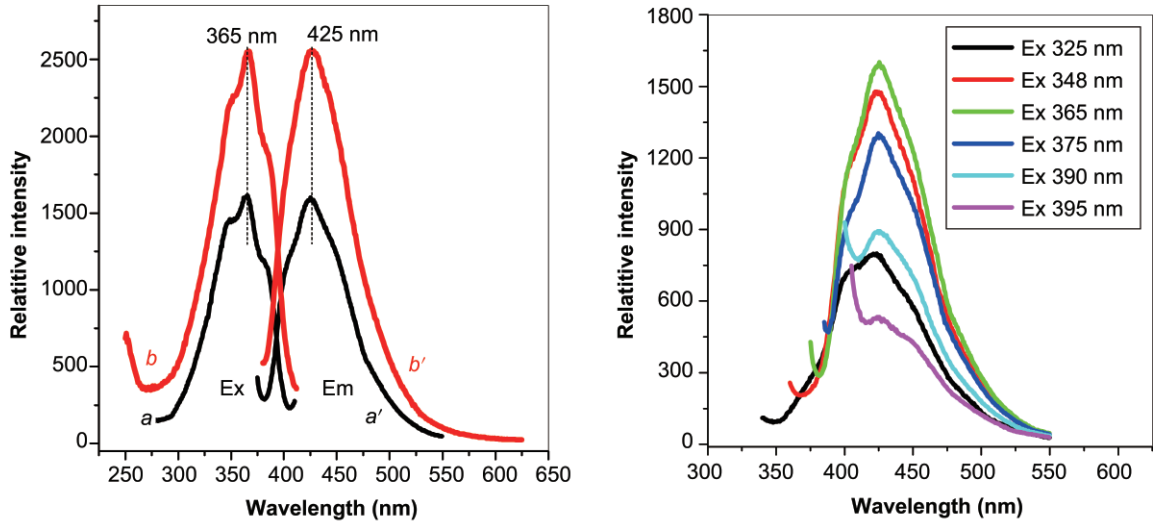

Figure 8 (a) Room temperature photoluminescence (PL) spectra of Sb_2O_3 nanobelts before (lines *a* and *a*′) and after calcination (lines *b* and *b*′). The spectra indicate that the PL excitation peaks (lines *a* and *b*) are at 365 nm, while the PL emission peaks (lines *a*′ and *b*′) are at 425 nm. (b) The photoluminescence emission spectra with various excitation wavelengths of Sb_2O_3 nanobelts before calcination

gap, and result in a strong photoluminescence signal at room temperature. Actually, there is a lack of investigation of luminescence in Sb_2O_3 systems so that the origin and the mechanism of the emission require further investigation, such as fluorescence lifetime measurements.

3. Conclusions

In summary, we have demonstrated that orthorhombic Sb_2O_3 nanobelts with unique elliptical cross sections and 3-D flower-like nanostructures built up from tens of nanobelts can be obtained from aqueous solution. Optical measurements reveal that the Sb_2O_3 nanobelts display intense purple-blue photoluminescence centered at 425 nm. We envisage that the as-obtained Sb_2O_3 nanobelts may be a potential new candidate for effective purple-blue light emitters, and might also be valuable for future theoretical research and nanodevice design. In addition, the present study may cast new light on the investigation of property differences between nanobelts with rectangular cross sections and elliptical cross sections. By suitable choice of source materials and synthesis parameters, it is reasonable to expect that the present study could be extended to the synthesis of other novel metal oxide nanobelts and the corresponding 3-D nanostructures.

Acknowledgements

We are grateful to Fee Li Lie at the University of Arizona for help with the XPS characterization and for financial support from the National Natural Science Foundation of China (Nos. 60736001, 60572031, and 20571080) and Science Foundation Arizona (Strategic Research Group Program).

Electronic Supplementary Material: Additional SEM and TEM images of Sb_2O_3 nanobelts with elliptical cross-section are available in the online version of this article at http://dx.doi.org/10.1007/s12274-009-9014-y and are accessible free of charge.

References

[1] Pan, Z. W.; Dai, Z. R.; Wang, Z. L. Nanobelts of semiconducting oxides. *Science* **2001**, *291*, 1947–1949.

[2] Shi, W.; Peng, H.; Wang, N.; Li, C. P.; Xu, L.; Lee, C. S.; Kalish, R.; Lee, S. T. Free-standing single crystal silicon nanoribbons. *J. Am. Chem. Soc.* **2001**, *123*, 11095–11096.

[3] Yu, Y.; Wang, R. H.; Chen, Q.; Peng, L. M. High-quality ultralong Sb_2S_3 nanoribbons on large scale. *J. Phys.*

Chem. B **2005**, *109*, 23312–23315.

[4] Hu, C. G.; Liu, H.; Dong, W. T.; Zhang, Y. Y.; Bao, G.; Lao, C. S.; Wang, Z. L. $La(OH)_3$ and La_2O_3 nanobelts—Synthesis and physical properties. *Adv. Mater*. **2007**, *19*, 470–474.

[5] Arnold, M. S.; Avouris, P.; Wang, Z. L. Field-effect transistors based on single semiconducting oxide nanobelts. *J. Phys. Chem. B* **2003**, *107*, 659–663.

[6] Comini, E.; Faglia, G.; Sberveglieri, G.; Pan, Z. W.; Wang, Z. L. Stable and highly sensitive gas sensors based on semiconducting oxide nanobelts. *Appl. Phys. Lett*. **2002**, *81*, 1869–1871.

[7] Bai, X. D.; Gao, P. X.; Wang, Z. L.; Wang, E. G. Dual-mode mechanical resonance of individual ZnO nanobelts. *Appl. Phys. Lett*. **2003**, *82*, 4806–4808.

[8] Hughes, W.; Wang, Z. L. Nanobelts as nanocantilevers. *Appl. Phys. Lett*. **2003**, *82*, 2886–2888.

[9] Yan, H.; Johnson, J.; Law, M.; He, R.; Knutsen, K.; McKinney, J. R.; Pham, J.; Saykally, R.; Yang, P. ZnO nanoribbon microcavity lasers. *Adv. Mater*. **2003**, *15*, 1907–1911.

[10] Xiong, Q. H.; Wang, J. G.; Reese, O.; Voon, L. C. L. Y.; Eklund, P. C. Raman scattering from surface phonons in rectangular cross-sectional w-ZnS nanowires. *Nano Lett*. **2004**, *4*, 1991–1996.

[11] Xia, Y. N.; Yang, P. D.; Sun, Y. G.; Wu, Y. Y.; Mayers, B.; Gates, B.; Yin, Y. D.; Kim, F.; Yan, Y. Q. Chemistry and physics of nanowires. *Adv. Mater.* **2003**, *15*, 353–389.

[12] Gao, P.; Wang, Z. L. Self-Assembled nanowire–nanoribbon junction arrays of ZnO. *J. Phys. Chem. B* **2002**, *106*, 12653–12658.

[13] Lao, J. Y.; Wen, G. J.; Ren, Z. F. Hierarchical ZnO nanostructures. *Nano Lett*. **2002**, *2*, 1287–1291.

[14] Liu, B.; Zeng, H. C. Fabrication of ZnO "dandelions" via a modified Kirkendall process. *J. Am. Chem. Soc*. **2004**, *126*, 16744–16746.

[15] Li, Z. Q.; Ding, Y.; Xiong, Y. J.; Yang, Q.; Xie, Y. One-step solution-based catalytic route to fabricate novel α-MnO_2 hierarchical structures on a large scale. *Chem. Commun*. **2005**, 918–920.

[16] Yao, W. T.; Yu, S. H.; Liu, S. J.; Chen, J. P.; Liu, X. M.; Li, F. Q. Architectural control syntheses of CdS and CdSe nanoflowers, branched nanowires, and nanotrees via a solvothermal approach in a mixed solution and their photocatalytic property. *J. Phys. Chem. B* **2006**, *110*, 11704–11710.

[17] Guo, L.; Wu, Z. H.; Liu, T.; Wang, W. D.; Zhu, H. S. Synthesis of novel Sb_2O_3 and Sb_2O_5 nanorods. *Chem. Phys. Lett*. **2000**, *318*, 49–52.

[18] Friedrichs, S.; Meyer, R. R.; Sloan, J.; Kirkland, A. I.; Hutchison, J. L.; Green, M. L. H. Complete characterisation of a Sb_2O_3/(21,–8)SWNT inclusion composite. *Chem. Commun*. **2001**, 929–930.

[19] Ye, C. H.; Meng, G. W.; Zhang, L. D.; Wang, G. Z.; Wang, Y. H. A facile vapor–solid synthetic route to Sb_2O_3 fibrils and tubules. *Chem. Phys. Lett*. **2002**, *363*, 34–38.

[20] Zhang, Y. X.; Li, G. H.; Zhang, J.; Zhang, L. D. Shape-controlled growth of one-dimensional Sb_2O_3 nanomaterials. *Nanotechnology* **2004**, *15*, 762–765.

[21] Chen, X. Y.; Wang, X.; An, C. H.; Liu, J. W.; Qian, Y. T. Synthesis of Sb_2O_3 nanorods under hydrothermal conditions. *Mater. Res. Bull*. **2005**, *40*, 469–474.

[22] Christian, P.; O'Brien, P. The preparation of antimony chalcogenide and oxide nanomaterials. *J. Mater. Chem*. **2005**, *15*, 4949–4954.

[23] Sendor, D.; Weirich, T.; Simon, U. Transformation of nanoporous oxoselenoantimonates into Sb_2O_3-nanoribbons and nanorods. *Chem. Commum*. **2005**, 5790–5792.

[24] Deng, Z. T.; Tang F. Q.; Chen D.; Meng X. W.; Cao, L.; Zou. B. S. A simple solution route to single-crystalline Sb_2O_3 nanowires with rectangular cross sections. *J. Phys. Chem. B* **2006**, *110*, 18225–18230.

[25] Chand, N.; Verma, S. Surface and strength properties of PVC-Sb_2O_3 flame retardant coated sunhemp fiber. *J. Fire Sci*. **1991**, *9*, 251–258.

[26] Sato, H.; Kondo, K.; Tsuge, S.; Ohtani, H.; Sato, N. Mechanisms of thermal degradation of a polyester flame-retarded with antimony oxide/brominated polycarbonate studied by temperature-programmed analytical pyrolysis. *Polym. Degrad. Stab*. **1998**, *62*, 41–48.

[27] Liu, H. H.; Iwasawa, Y. Unique performance and characterization of a crystalline $SbRe_2O_6$ catalyst for selective ammoxidation of isobutane. *J. Phys. Chem. B* **2002**, *106*, 2319–2329.

[28] Ha, Y.; Wang, M. Capillary melt method for micro antimony oxide pH electrode. *Electroanalysis* **2006**, *18*, 1121–1125.

[29] Deng, Z. T.; Chen, D.; Tang, F. Q.; Meng, X. W.; Ren, J.; Zhang, L. Orientated attachment assisted self-assembly of Sb_2O_3 nanorods and nanowires: End-to-end versus side-by-side. *J. Phys. Chem. C*. **2007**, *111*, 5325–5330.

[30] Deng, Z. T.; Peng, B.; Chen, D.; Tang, F. Q.; Muscat, A. J. A new route to self-assembled tin dioxide nanospheres: Fabrication and characterization. *Langmuir*; **2008**, *24*, 11089–11095.

[31] Deng, Z. T.; Chen, D.; Peng, B.; Tang, F. Q. From bulk metal Bi to two-dimensional well-crystallized BiOX (X=Cl, Br) micro- and nanostructures: Synthesis and characterization. *Cryst. Growth Des*. **2008**, *8*, 2995–3003.

[32] Deng, Z. T.; Tang, F. Q.; Muscat, A. J. Strong blue photoluminescence from single-crystalline bismuth oxychloride nanoplates. *Nanotechnology* **2008**, *19*, 295705.

[33] Wagner, C. D. Sensitivity factors for XPS analysis of surface atoms. *J. Electron Spectrosc. Relat. Phenom*. **1983**, *32*, 99–102.

[34] Moulder, J.; Stickie, W.; Sobal, P.; Bomber, K. *Handbook of X-ray Photoelectron Spectroscopy*; Perkin Elmer: Eden Prairie, MN, 1992.

[35] Liu, K. S.; Zhai, J.; Jiang, L. Fabrication and characterization of superhydrophobic Sb_2O_3 films. *Nanotechnology*, **2008**, *19*, 165604.

[36] Cody, C. A.; DiCarlo, L.; Darlington, R. K. Vibrational and thermal study of antimony oxides. *Inorg. Chem*. **1979**, *18*, 1572–1576.

[37] Mestl, G.; Ruiz, P.; Delmon, B.; Knozinger, H. Sb_2O_3/Sb_2O_4 in reducing/oxidizing environments: *An in situ* Raman spectroscopy study. *J. Phys. Chem*. **1994**, 11276–11282.

[38] Liu, B.; Zeng, H. C. Hydrothermal synthesis of ZnO nanorods in the diameter regime of 50 nm. *J. Am. Chem. Soc*. **2003**, *125*, 4430–4431.

[39] Mayers, B.; Gates, B.; Yin, Y. D.; Xia, Y. N. Large-scale synthesis of monodispersed nanorods of Se/Te alloys through a homogeneous nucleation and solution growth process. *Adv. Mater*. **2001**, *13*, 1380–1384.

[40] Liu, Z. P.; Peng, S.; Xie, Q.; Hu, Z. K.; Yang, Y.; Zhang, S. Y.; Qian, Y. T. Large-scale synthesis of ultralong Bi_2S_3 nanoribbons via a solvothermal process. *Adv. Mater*. **2003**, *15*, 936–940.

[41] Che, R, C.; Peng, L. M.; Zhou, W. Z. Synthesis and characterization of crystalline microporous cobalt phosphite nanowires. *Appl. Phys. Lett*. **2005**, *87*, 173122.

[42] Hsu, J. W. P.; Tallant, D. R.; Simpson, R. L.; Missert, N. A.; Copel, R. G. Luminescent properties of solution-grown ZnO nanorods. *Appl. Phys. Lett*. **2006**, *88*, 252103.

[43] Her, Y. C.; Wu, J. Y.; Lin, Y. R.; Tsai, S. Y. Low-temperature growth and blue luminescence of SnO_2 nanoblades. *Appl. Phys. Lett*. **2006**, *89*, 043115.